MOOG LADDER FILTER GENERALIZATIONS BASED ON STATE VARIABLE FILTERS

Kurt James Werner and Russell McClellan

iZotope, Inc., Cambridge, MA

{kwerner|rmcclellan}@izotope.com

ABSTRACT

We propose a new style of continuous-time filter design composed of a cascade of 2nd-order state variable filters (SVFs) and a global feedback path. This family of filters is parameterized by the SVF cutoff frequencies and resonances, as well as the global feedback amount. For the case of two identical SVFs in cascade and a specific value of the SVF resonance, the proposed design reduces to the well-known Moog ladder filter. For another resonance value, it approximates the Octave CAT filter. The resonance parameter can be used to create new filters as well. We study the pole loci and transfer functions of the SVF building block and entire filter. We focus in particular on the effect of the proposed parameterization on important aspects of the filter's response, including the passband gain and cutoff frequency error. We also present the first in-depth study of the Octave CAT filter circuit.

1. INTRODUCTION

The Moog ladder filter [1, 2] was a landmark electronic music design. It is a cascade of four identical 1st-order low-pass filters with global feedback. It has been studied extensively in the virtual analog literature, e.g. [3–9]. It also inspired a number of other circuit designs including higher-order generalizations of the Moog filter [8, 9] and "polygon filters" [4, 10–13]. Zavalishin [13] studied some modifications to the Moog ladder filter, including a "true high-pass" mode, "true band-pass" mode, and adding damping controls to 2nd-order band-pass blocks.

The Moog ladder filter is not the only classic filter design built from identical 1st-order filters. Filters made up of four cascaded sections of integrator-based low-pass filters with variable global feedback are common in commercial synthesizer designs. The datasheets for the CEM3320 [14] and SSM2040 [15] voltage-controlled filter integrated circuits recommended this topology.

Many synthesizers that contained these integrated circuits used this topology, notably including the Sequential Circuits Prophet 5 [16] and Oberheim OB-Xa [17], both early commercial polyphonic synthesizers. Roland Corporation commercialized many designs based on this topology, including in their first polyphonic synthesizer, the Jupiter 4 [18].

These 1st-order filter blocks are implemented using op-amps, Moog's original discrete-transistor design [1, 2], or diodes [19]. Transconductance-amplifier-based designs [20–26], where the amplifier controls the cutoff frequency, are common.

Another standard, 2nd-order, filter in electronic music is the state variable filter (SVF). Filters based on cascaded SVF sections
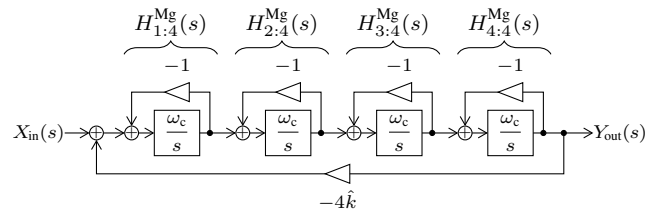
Figure 1: *Full Moog ladder filter block diagram.*

are also common in commercial designs. Notable examples include the Yamaha CS series [27], a line of early polyphonic synthesizers, and later Roland Corp. polyphonic models including the Jupiter 6 [28]. The Octave CAT [25, 29] uses two SVFs in cascade, surrounded by a global negative feedback, like the Moog.

In this paper, we introduce a novel continuous-time filter design which replaces each pair of low-pass filters in the Moog ladder filter with an SVF. This has a new degree of freedom: the SVF damping. This can be seen as filling the gaps between Moog's original design, the Octave CAT, and Zavalishin's proposed variants, to a fully-parameteric SVF-core 4-pole filter. We study the pole loci, magnitude responses, and some time-domain behavior of this new filter, its stability bounds, and the error of its leading pole frequency.

In the following, we first review the Moog ladder filter (§2) and analyze the circuit of the Octave CAT filter (§3). We propose the new generalization (§4) of these filters, study its continuous-time state space and time-varying behavior (§5), and show a discrete-time implementation (§6).

2. MOOG LADDER FILTER

First, we review the Moog low-pass ladder filter. Its circuit analysis is well-represented in the literature (e.g. [3, 8, 9, 30]). We just review its pole parameterization and conditions on its stability.

The Moog ladder filter is composed of four identical blocks, indexed by $i \in \{1, 2, 3, 4\}$, with transfer functions

$$H_{i:4}^{\text{Mg}}(s) = Y_{i:4}^{\text{Mg}}(s)/X_{i:4}^{\text{Mg}}(s) = \omega_{\text{c}}/(s + \omega_{\text{c}}), \quad (1)$$

where ω_{c} is the cutoff frequency in radians. ω_{c} depends on the electronic circuit parameters and an applied control signal [8].

The input to the first block is $X_{1:4}^{\text{Mg}}(s) = X_{\text{in}}(s) - 4\hat{k}Y_{4:4}^{\text{Mg}}(s)$, where $0 \leq \hat{k} \leq 1$ is a "normalized" feedback gain[1], $\hat{k} = 0$ is no feedback and $\hat{k} = 1$ is the edge of stability. The inputs to the other three, $i \in \{2, 3, 4\}$, are $X_{i:4}^{\text{Mg}}(s) = Y_{i-1:4}^{\text{Mg}}(s)$. The output is $Y_{\text{out}}(s) = Y_{4:4}^{\text{Mg}}(s)$.

---

[1] Typically, an "unnormalized" coefficient $k = 4\hat{k}$ is used [8].
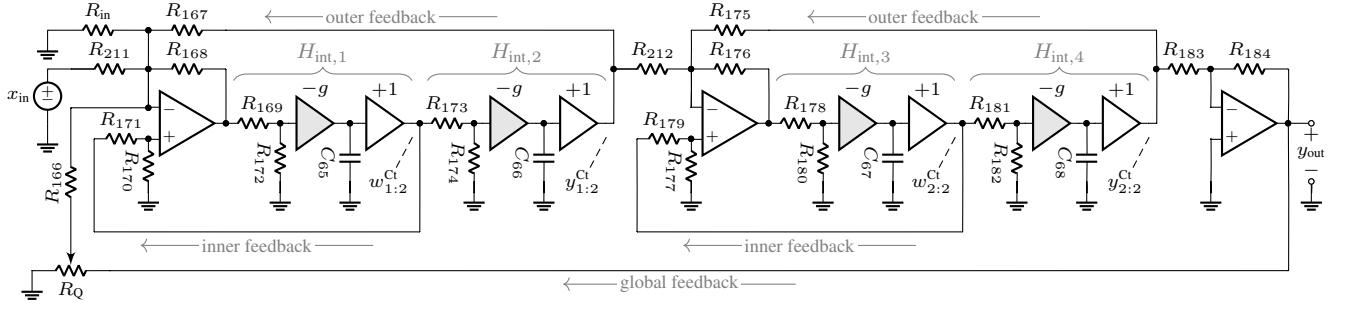
Figure 2: *Octave CAT filter schematic [25], including Keller's correction [29].*

Fig. 1 shows the Moog block diagram. Its transfer function is

$$H_{\text{io},4}^{\text{Mg}}(s) = \frac{Y_{\text{out}}(s)}{X_{\text{in}}(s)} = \frac{\prod\limits_{i=1}^{4} H_{i:4}^{\text{Mg}}(s)}{1 + 4\hat{k}\prod\limits_{i=1}^{4} H_{i:4}^{\text{Mg}}(s)} \, . \tag{2}$$

This can be rewritten as

$$H_{\text{io},4}^{\text{Mg}}(s) = \frac{\omega_{\text{c}}^4}{\prod\limits_{\psi \in \pm 1} \prod\limits_{\phi \in \pm 1} s + \omega_{\text{c}}\left(1 + \phi\sqrt{2}\sqrt[4]{\hat{k}}e^{j\psi\pi/4}\right)} \, , \tag{3}$$

showing that $H_{\text{io},4}^{\text{Mg}}(s)$ has 4 poles at $s = p_{\psi,\phi}^{\text{Mg}}$, with $\psi, \phi \in \pm 1$. $+1$ and -1 are abbreviated in subscripts as $+$ and $-$ for compactness. Here, ϕ denotes which conjugate pole pair is being considered, and ψ denotes whether its positive ($\Im\{p_{\psi,\phi}^{\text{Mg}}\} \geq 0$) or negative ($\Im\{p_{\psi,\phi}^{\text{Mg}} \leq 0$) member is being considered. These poles $p_{\psi,\phi}^{\text{Mg}} = \sigma_{\psi,\phi} + \omega_{\psi,\phi}j$ have real and imaginary parts

$$\sigma_{\psi,\phi} = \omega_{\text{c}}\left(\psi\sqrt[4]{\hat{k}} - 1\right) \tag{4}$$

$$\omega_{\psi,\phi} = \omega_{\text{c}}\left(\phi\sqrt[4]{\hat{k}}\right) \, . \tag{5}$$

Poles $p_{+,+}^{\text{Mg}}$ and $p_{+,-}^{\text{Mg}}$ form a conjugate pair ($p_{+,+}^{\text{Mg}} = \bar{p}_{+,-}^{\text{Mg}}$), as do $p_{-,+}^{\text{Mg}}$ and $p_{-,-}^{\text{Mg}}$ ($p_{-,+}^{\text{Mg}} = \bar{p}_{-,-}^{\text{Mg}}$). The pole loci are red (——) in Fig. 8.

Passband gain g_{dc} is an important measure of its behavior [8, 20], found by evaluating (2) at $s = 0$:

$$g_{\text{dc}} = 1/(1 + 4\hat{k}) \, . \tag{6}$$

The passband gain g_{dc} varies between 1.0 (0 dB) when $\hat{k} = 0$ and 0.2 (≈ -14 dB) when $\hat{k} = 1$. The changing passband gain is seen in a family of magnitude responses ($\hat{k} \in [0, 1]$), shown in Fig. 9.

2.1. Stability analysis

The Moog is stable when all of its poles lie in the left half s-plane:

$$\sigma_{\pm,\pm} < 0 \, . \tag{7}$$

Since the "leading" poles[2] $p_{+,\pm}$ always have the more positive real part, i.e. $\sigma_{+,\pm} \geq \sigma_{-,\pm}$, we can consider only the leading

---

[2]Sometimes these are called the "dominant" poles [3, 4, 31, 32], but we will avoid that terminology for its risk of confusion with the "dominant pole" in op-amp circuit design.

Table 1: *CAT components (left) and derived quantities (right).*

component	val.	unit	quantity	val.	unit
$R_{172}, R_{174}, R_{180}, R_{182}$	220	Ω	R_{in}	49.7	kΩ
R_{171}, R_{179}	4.7	kΩ	$R_{\|,1:2}$	4.35–4.76	kΩ
$R_{\text{Q}}, R_{166}\text{–}R_{170}, R_{173},$ $R_{175}\text{–}R_{178}, R_{181},$ $R_{183}, R_{184}, R_{212}$	10	kΩ	$R_{\|,2:2}$	5	kΩ
			$r_{1:2}$	1.05–1.12	—
			$r_{2:2}$	1.02	—
R_{163}	47	kΩ	k	[0.0, 1.0]	—
R_{162}, R_{211}	100	kΩ	γ_0	0.1	—
R_{164}, R_{165}	150	kΩ	$a_{1:2}, a_{2:2},$ γ_1, γ_2	1.0	—
$C_{65}\text{–}C_{68}$	100	nF			

poles ($\psi = +1$). Since all of the poles exist in complex conjugate pairs, it is sufficient to study either $\phi = \pm 1$; we arbitrarily choose $\phi = +1$. So, satisfying (7) reduces to satisfying

$$\sigma_{+,+} < 0 \, . \tag{8}$$

This is satisfied for $0 \leq \hat{k} < 1$.

3. OCTAVE CAT FILTER

The Octave CAT schematic, taken from the service notes [25] and a correction by Keller [29], is shown in Fig. 2 with component values given in Tab. 1. In this figure, shaded gray triangles with one input represent (inverting) transconductance amplifiers and empty triangles with one input represent (unity gain) voltage buffers.[3] Examining this circuit reveals that the circuit can be analyzed as a feedback network of inverting and non-inverting voltage summers, voltage amplifiers, and voltage integrators arranged in the form of the block diagram in Fig. 3.

After analyzing that block diagram, we will derive its particulars in terms of the electronic circuit values.

3.1. Functional analysis

Like the Moog, the Octave CAT filter contains several filter blocks in cascade, surrounded by global feedback. It has two *nearly* identical blocks (indexed by $i \in \{1, 2\}$) with transfer functions

$$H_{i:2}^{\text{Ct}}(s) = Y_{i:2}^{\text{Ct}}(s)/X_{i:2}^{\text{Ct}}(s) = \frac{\omega_{\text{c}}^2}{s^2 + 2r_{i:2}\omega_{\text{c}}s + \omega_{\text{c}}^2} \, . \tag{9}$$

---

[3]Here, we assume ideal behavior for these amplifiers, although of course more refined models exist and can be useful [33–35].
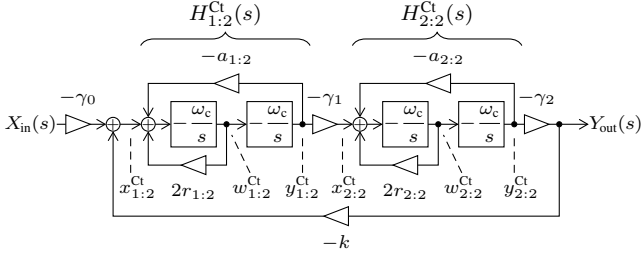
Figure 3: *Octave CAT filter block diagram.*

(a) One of four stages.   (b) Detail on one stage.

Figure 4: *Octave CAT integrator subcircuit.*

The input to the first block is defined by $X_{i:2}^{Ct}(s) = X_{in}(s) - \frac{\hat{k}}{\sqrt{2}} Y_{2:2}^{Ct}(s)$, where again $0 \leq \hat{k} \leq 1$ is the "normalized" feedback with the same meaning as before. The input to the second stage is defined by $X_{2:2}^{Ct}(s) = Y_{1:2}^{Ct}(s)$. The output is defined by $Y_{out}(s) = Y_{2:2}^{Ct}(s)$.

The Octave CAT's transfer function is

$$H_{io,4}^{Ct}(s) = \frac{Y_{out}(s)}{X_{in}(s)} = \frac{\prod_{i=1}^{2} H_{i:2}^{Ct}(s)}{1 + \frac{\hat{k}}{\sqrt{2}} \prod_{i=1}^{2} H_{i:2}^{Ct}(s)} \qquad (10)$$

Unfortunately, past this point the case $r_{1:2} \neq r_{2:2}$ is not tractable. So, we make the light assumptions that $r_{1:2} = r_{2:2} = r \approx 1.064$, calling this approximation "≈CAT." Fig. 8 shows the pole loci for "≈CAT" (——) and the exact CAT (······). Notice that especially for the leading pole pair, the match is very close.

Fig. 9 shows a family of magnitude responses for ≈CAT and the exact CAT. Notice again that the match is very close. This also shows a few differences between the exact CAT and ≈CAT and the Moog filter. The resonance for the exact CAT never goes above 0 dB, while the Moog filter's resonance can go to ∞ (self-oscillation). g_{dc} for the exact CAT never goes as low as for the Moog. Conversely, ≈CAT, whose global feedback can go higher, is able to get a lower g_{dc} than the Moog: ≈ -15 dB when $\hat{k} = 1$.

3.2. Circuit analysis

Here, we analyze the Octave CAT filter's circuit in more detail, deriving parameter values for our block diagram and justifying the choice of $r \approx 1.064$ for ≈CAT.

The Octave CAT filter has four inputs, coming from the synthesizer's noise source, two VCOs, and external audio input[4]. We study the filter's behavior from the perspective of the external audio input, assuming the other 3 inputs are at ground and bundling their resistances (not shown) into a single resistor

$$R_{in} = (R_{162} + R_{163})||R_{164}||R_{165}, \qquad (11)$$

where || indicates putting two impedances in parallel[5]. For the actual component values, $R_{in} \approx 49.7$ kΩ. The filter's input gain is found by analyzing its input stage as an inverting amplifier

$$-\gamma_0 = -\frac{R_{168}}{R_{211}}, \qquad (12)$$
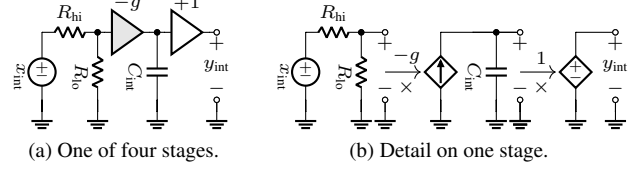
yielding $\gamma_0 = 0.1$. Notice that the choice of input only affects scaling, not the dynamics of the filter (i.e., pole positions).

The four identical integrators in the CAT are built from transconductance amplifiers, voltage buffers, and a few passive components each. A single integrator from the CAT is shown in Fig. 4a. Assuming high input impedance on the buffer and high output impedance on the OTA, the basic building block is approximated by Fig. 4b. Simple nodal analysis gives this integrator subcircuit's transfer function as

$$H_{int}(s) = \frac{Y_{int}(s)}{X_{int}(s)} = \frac{\omega_c}{s}, \quad \text{with } \omega_c = \frac{g R_{lo}}{(R_{lo} + R_{hi})C_{int}}. \qquad (13)$$

The SSM2040 datasheet gives a nominal transconductance range of $1/500000 \leq g \leq 1/50$ ℧ (mhos), allowing us to estimate a range of cutoff frequencies for the actual Octave CAT circuit: $39 \lesssim f_c \lesssim 391389$ Hz. The "global" feedback gain k set by a voltage divider and inverting amplifier is

$$k = -\frac{R_{168} R_{Q,-}}{R_{166} R_Q + R_{Q,+} R_{Q,-}}, \qquad (14)$$

where $R_{Q,+}, R_{Q,-} \in [0, R_Q]$ are the two halves of the potentiometer R_Q (they also satisfy $R_{Q,-} + R_{Q,+} = R_Q$). k varies between 0.0 (when $R_{Q,-} = 0$ and $R_{Q,+} = R_Q$) and 1.0 (when $R_{Q,-} = R_Q$ and $R_{Q,-} = 0$).

Each integrator pair ($H_{int,1}$ and $H_{int,2}$ resp. $H_{int,3}$ and $H_{int,4}$) is combined with a summing amplifier to make two state variable filters (SVFs). The two SVF stages in the Octave CAT are nearly identical. The "outer" feedback loop gains $a_{1:2}$ and $a_{2:2}$ can be found by analyzing the circuits as inverting amplifiers,

$$-a_{1:2} = -R_{168}/R_{167}, \quad -a_{2:2} = -R_{176}/R_{175},$$

yielding $a_{1:2} = a_{2:2} = 1.0$.

The "inner" feedback loop of each SVF can be analyzed as a voltage divider feeding a non-inverting amplifier with a total gain of $2 r_{i:2}, i \in \{1, 2\}$, with

$$r_{1:2} = \frac{R_{170}}{R_{170} + R_{171}} \left(1 + \frac{R_{168}}{R_{||,1:2}}\right) \Big/ 2 \qquad (15)$$

$$r_{2:2} = \underbrace{\frac{R_{177}}{R_{177} + R_{179}}}_{\text{voltage divider}} \underbrace{\left(1 + \frac{R_{176}}{R_{||,2:2}}\right)}_{\text{non-inverting amp.}} \Big/ 2. \qquad (16)$$

Notice that the voltage divider terms are both ≈ 0.68 and $R_{168} = R_{176}$. $R_{||,1:2}$ and $R_{||,2:2}$ are parallel combinations of op-amp inverting inputs' other input resistances, specifically

$$R_{||,1:2} = R_{in}||(R_{166} + R_{Q,+}||R_{Q,-})||R_{167}||R_{211} \qquad (17)$$

$$R_{||,2:2} = R_{175}||R_{212}. \qquad (18)$$

---

[4]For simplicity, we omit dc coupling capacitor C_{64} on the audio input.
[5]For impedances R_α and R_β, $R_\alpha||R_\beta = R_\alpha R_\beta / (R_\alpha + R_\beta)$.
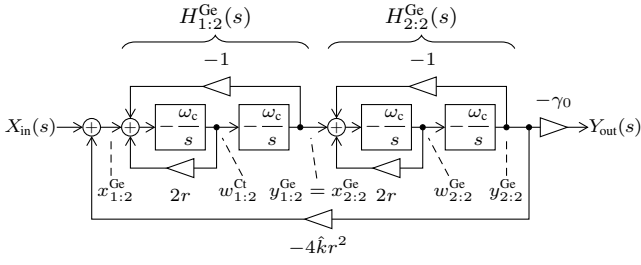
Figure 5: *Full Proposed Generalized filter block diagram.*

Noting that $0 \leq R_{Q,-} || R_{Q,+} \leq R_Q/4$, we see that depending on the position of the R_Q potentiometer, we find an "inner" feedback gain $r_{1:2}$ between 1.05–1.12 for the first SVF. The "inner" feedback gain $r_{2:2}$ of the second SVF is 1.02. Notice that it is only because $R_{||,1:2} \neq R_{||,2:2}$ that $r_{1:2} \neq r_{2:2}$.

Finally, the output gains of each SVF, γ_1 and γ_2, are found by applying inverting amplifier equations,

$$-\gamma_1 = -\frac{R_{176}}{R_{212}}, \quad -\gamma_2 = -\frac{R_{184}}{R_{183}},$$

yielding $\gamma_1 = 1.0$ and $\gamma_2 = 1.0$.

3.3. Stability analysis

The CAT is stable when all of its poles lie in the left half s-plane:

$$\sigma_{\pm,\pm}^{Ct} < 0. \tag{19}$$

This holds for the exact CAT for all knob positions of R_Q, and for $\approx$CAT when $0 \leq \hat{k} < 1$.

4. PROPOSED GENERALIZED FILTER

We propose that $\approx$CAT can be generalized by allowing the SVF damping parameter r to vary freely. The proposed generalized block diagram is shown in Fig. 5. Its transfer function is

$$H_{io,4}^{Ge}(s) = \frac{Y_{out}(s)}{X_{in}(s)} = \frac{-\gamma_0 \prod_{i=1}^{2} H_{i:2}^{Ge}(s)}{1 + 4\hat{k}r^2 \prod_{i=1}^{2} H_{i:2}^{Ge}(s)}. \tag{20}$$

Here, $H_{i:2}^{Ge}(s)$ ($i \in \{1, 2\}$) is the classic low-pass state-variable filter (SVF) with transfer function

$$H_{i:2}^{Ge}(s) = \frac{\omega_c^2}{s^2 + 2r\omega_c s + \omega_c^2}, \tag{21}$$

where ω_c is the cutoff frequency in radians and r is the "damping." $H_{i:2}^{Ge}(s)$ has two poles at

$$p_{\pm}^{SVF} = \omega_c \left(-r \pm \sqrt{r^2 - 1}\right). \tag{22}$$

For $0 \leq r < 1$ these are a complex conjugate pair. For $r = 1$ the poles are coincident at $s = -\omega_c$. For $1 < r$, they are a pair of poles on the real axis spaced reciprocally around the point $s = -\omega_c r$. Fig. 6 shows the pole loci for $H_{i:2}^{Ge}(s)$, with the complex conjugate branch in blue (——) and the real pair branch in green (——). A
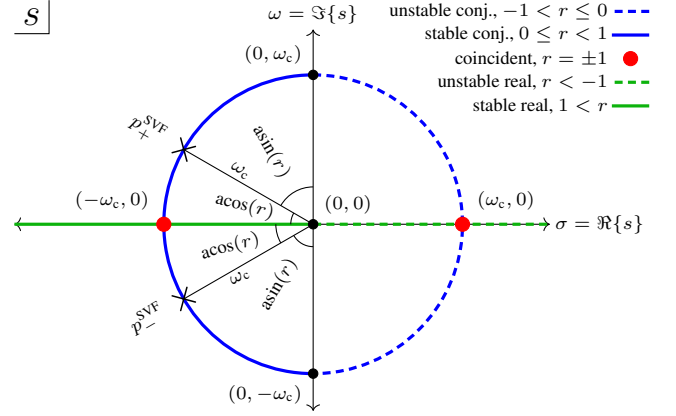
Figure 6: *Low-pass SVF pole loci.*

Table 2: *Setting parameters of the proposed generalized filter to match the Moog filter and (very nearly) the Octave CAT.*

val.	Moog	$\approx$CAT	Chebyshev	Butterworth	Bessel
γ_0	$+1$	-0.1	± 1	± 1	± 1
r	1	1.02–1.12	0.911	$1/\sqrt{2}$	$1/2$
k	$[0, 4[$	$[0, 1]$	$[0, 1.098]$	$[0, \sqrt{2}[$	$[0, 2[$
$\hat{k}$	$[0, 1[$	$[0, 0.22$–$0.25]$	$[0, 1[$	$[0, 1[$	$[0, 1[$

pair of conjugate poles $p_{\pm}^{SVF}$ are shown with two crucial features marked: their undamped natural frequency ω_c (pole radius) and the trigonometric relationship between the poles' angles from the real axis and their damping factor r. The SVF is only stable for $r \geq 0$, so we enforce that condition throughout.

Returning to the overall transfer function, $H_{io,4}^{Ge}(s)$ can be written to show its two pairs of conjugate poles as

$$H_{io,4}^{Ge}(s) = \frac{-\gamma_0 \omega_c^4}{\prod_{\psi \in \pm 1} \prod_{\phi \in \pm 1} s + \omega_c \left(r + \phi \sqrt[4]{\rho} e^{j\psi\theta}\right)}, \tag{23}$$

$$\text{where:} \begin{cases} \rho = \sigma_1^2 + \omega_1^2, \quad \sigma_1 = r^2 - 1, \quad \omega_1 = 2\sqrt{\hat{k}}r \\ \theta = -j\ln\left(\frac{\sigma_1 + \omega_1 j}{|\sigma_1 + \omega_1 j|}\right)/2 = \operatorname{atan}[\omega_1/\sigma_1]/2 \end{cases}.$$

This expression[6] leads to four poles $p_{\psi,\phi}^{Ge}$, with $\psi, \phi \in \pm 1$.

Poles $p_{\psi,\phi}^{Ge} = \sigma_{\psi,\phi} + \omega_{\psi,\phi}j$ have real and imaginary parts

$$\sigma_{\psi,\phi} = \omega_c \left[\left(\psi\sqrt{|\sigma_1 + \omega_1 j| + \omega_1^2}\right)/\sqrt{2} - r\right] \tag{24}$$

$$\omega_{\psi,\phi} = \omega_c \left(\phi\sqrt{|\sigma_1 + \omega_1 j| - \omega_1^2}\right)/\sqrt{2}. \tag{25}$$

Poles $p_{+,+}^{Ge}$ and $p_{+,-}^{Ge}$ form a conjugate pair; $p_{+,+}^{Ge} = \overline{p}_{+,-}^{Ge}$ since $\sigma_{+,+} = \sigma_{+,-}$ and $\omega_{+,+} = -\omega_{+,-}$. Also, poles $p_{-,+}^{Ge}$ and $p_{-,-}^{Ge}$ form a conjugate pair; $p_{-,+}^{Ge} = \overline{p}_{-,-}^{Ge}$ since $\sigma_{-,+} = \sigma_{-,-}$ and $\omega_{-,+} = -\omega_{-,-}$. We pay particular attention to the poles $p_{+,-}^{Ge}$ and $p_{+,+}^{Ge}$, the "*leading* poles" [8]: those which are always the closest to the imaginary axis $\sigma \equiv 0$ (since $\sigma_{+,\pm} \geq \sigma_{-,\pm}$).

---

[6]The arctangent function here should, be implemented as a two-
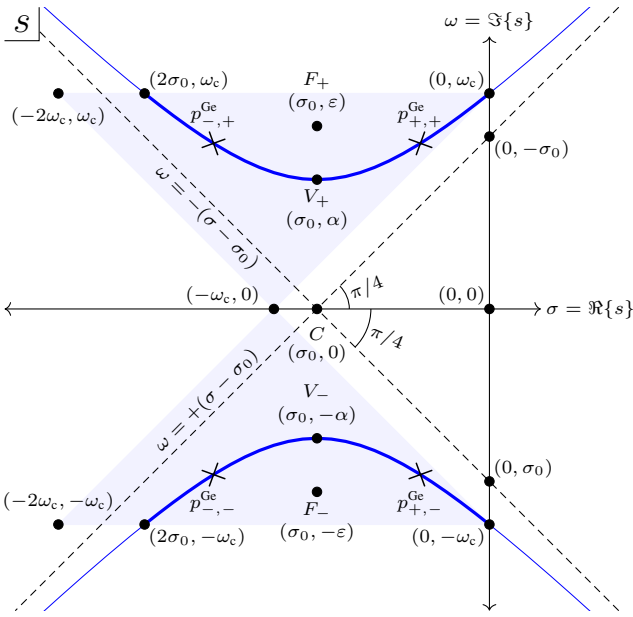
Figure 7: *North–South hyperbola loci.*

Figure 8: *Family of hyperbolic loci. Thick lines are stable poles $(0 \leq \hat{k} < 1)$ and thin lines are unstable poles $(1 < \hat{k})$. Blue lines are North–South hyperbolas $(0 \leq r < 1)$, green lines are East–West hyperbolas $(1 < r)$ and red lines are the degenerate case $(r = 1$, Moog filter). Dashed lines are the path traced by the hyperbola vertices $(\hat{k} = 0)$, cf. Fig. 6.*

Notice that[7] when $r = 1$, we have $\sigma_1 = 0$ and $\omega_1 = 2\sqrt{\hat{k}}$, giving us $\rho = 4\hat{k}$ and $\theta = \pi/2$, and recovering the Moog pole positions (4)–(5). With $r \approx 1.064$, the generalized filter matches $\approx$CAT. Tab. 2 summarizes other instances of the proposed generalized design, including those where the SVFs are tuned to match 2nd order Bessel, Butterworth, and Chebyshev type I designs.

Notice that $\hat{k} = 0$ (no global feedback) gives $\omega_1 = 0$, hence $\theta = 0$: each pair of poles ($\psi = \pm 1$) is coincident.

Notice finally that when $\hat{k} = 1$, we have $\omega_1 = 2r$ and hence $\rho = (r^2 + 1)^2$. This cancels the real part of the leading poles, $\sigma_{+,\pm} = 0$, meaning that the filter is conditionally stable with an oscillatory component at frequency $\omega_{+,\pm} = \omega_c$. This property was noted for the particular case of the 4th-order Moog filter (i.e., $r = 1$) in [8]; Here we show that it holds for *all* values of r.

As with the Moog filter, we can derive an expression for the passband gain g_{dc} by evaluating (23) at $s = 0$

$$g_{dc} = -\gamma_0/(1 + 4\hat{k}r^2).\quad(26)$$

Notice that, in general, the passband gain is affected by r. When $\hat{k} = 0$, it is simply $-\gamma_0$; when $\hat{k} = 1$, it is at its minimum value $-\gamma_0/(1 + r^2)$. As r increases, the minimum gets smaller and smaller. You can see this for a range of filters in the family of magnitude responses in Fig. 9.

4.1. Hyperbolic pole loci

For $0 < r < 1$, the pole loci of (23) are a hyperbola

$$\frac{\omega^2}{\alpha^2} - \frac{(\sigma - \sigma_0)^2}{\alpha^2 - \varepsilon^2} = 1,\quad(27)$$

where $\sigma = \Re\{s\}$ and $\omega = \Im\{s\}$, i.e., $s = \sigma + j\omega$. This "North–South" hyperbola is symmetrical around the lines $\sigma \equiv \sigma_0$ and $\omega \equiv 0$ and has a semi-major axis length α and a focal distance (linear eccentricity) ε. That is, this hyperbola has a center C at $(\sigma_0, 0)$, foci $F_\pm$ at $(\sigma_0, \pm\varepsilon)$, and vertices $V_\pm$ at $(\sigma_0, \pm\alpha)$.

Our hyperbola has

$$\sigma_0 = -\omega_c r, \quad \alpha = \omega_c\sqrt{1 - r^2}, \quad \varepsilon = \omega_c\sqrt{2(1 - r^2)}.\quad(28)$$

Hyperbolas have asymptotes at $\omega = \pm(\sqrt{\varepsilon^2 - \alpha^2})/\alpha)(\sigma - \sigma_0)$; this hyperbola has asymptotes at $\omega = \pm(\sigma - \sigma_0)$. This is a very particular type called a "rectangular hyperbola," one with an eccentricity of $\varepsilon/\alpha = \sqrt{2}$. Just like the specific case of the Moog filter, these asymptotes are offset from the real axis by an angle of $\pi/4$ and are perpendicular to one another. However, they translate along the real axis as a function of the SVF feedback r and cutoff frequency ω_c; recall (28). Notably, the asymptotes intersect the ω-axis at $(0, \mp\sigma_0)$, and the hyperbola intersects the ω-axis at $(0, \pm\omega_c)$. This means that, $\forall r, \hat{k} = 1$ corresponds to a conjugate poles pair *exactly* at the design frequency: $p_{+,\pm}^{Ge} = \pm\omega_c j$.

The hyperbola's full equation is

$$\frac{\omega^2}{\omega_c^2(1 - r^2)} - \frac{(\sigma + \omega_c r)^2}{\omega_c^2(1 - r^2)} = 1.\quad(29)$$

It is shown, with critical points labelled, in Fig. 7. Here, the asymptotes are dashed lines (- - -), the hyperbolas for $0 \leq \hat{k} < 1$ (all stable) are thick blue lines (——), and the hyperbolas for $\hat{k} < 0 \lor 1 \geq \hat{k}$ (at least one unstable) are thin blue lines (——). The shaded region shows the range of possible pole locations for $0 \leq \hat{k} < 1$ and $0 \leq r \leq 1$.

---

argument version, often called "atan2()." Typical usage for our equation here would be "atan2$(2r\sqrt{\hat{k}}, r^2 - 1)$."

[7]Recall that $\lim_{x\to+\infty}[\text{atan}(x)] = \pi/2$.
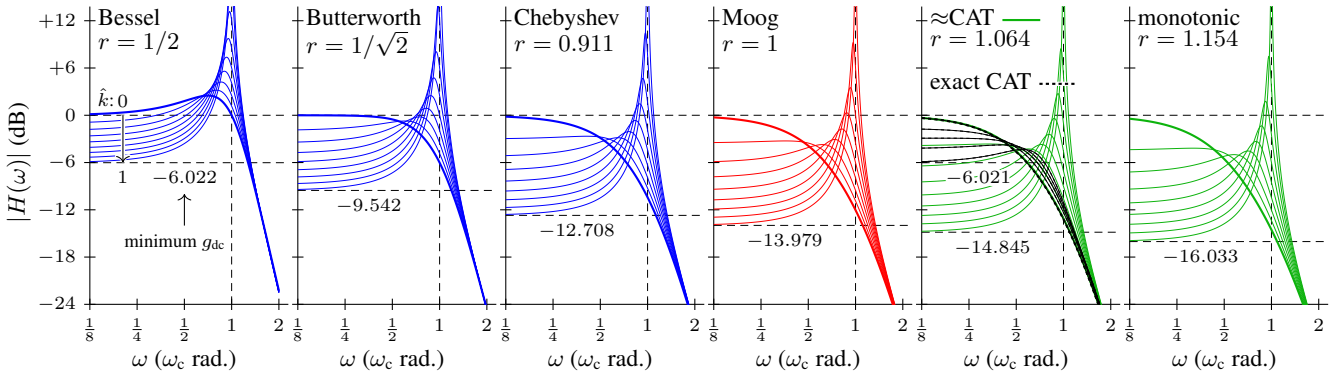
Figure 9: *Magnitude responses of various filters for $\hat{k} \in \{0, 1/8, \ldots, 7/8, 1\}$. Thick line represents $\hat{k} = 0$.*
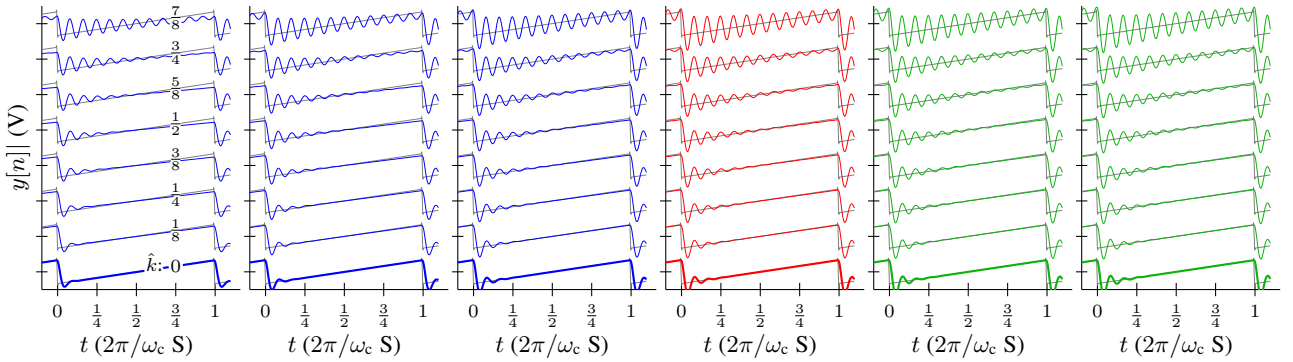
Figure 10: *Time domain responses to a sawtooth wave of frequency $\omega_c/12$ for $\hat{k} \in \{0, 1/8, \ldots, 6/8, 7/8\}$. Vertical offset added for clarity.*

Fig. 7 also shows which portions of the hyperbola are traversed by which pole. The positive leading pole $p_{+,+}^{\mathrm{Ge}}$ occupies the branch to the right of V_+. The negative leading pole $p_{+,-}^{\mathrm{Ge}}$ occupies the branch to the right of V_-. The non-leading poles $p_{-,\pm}^{\mathrm{Ge}}$ occupy the branches to the left of $V_\pm$. Recall that the exact locations of all these poles are given by (24)–(25). For stable filters $0 \leq \hat{k} < 1$, the leading poles $p_{+,\pm}$ always satisfy $\sigma_0 < \sigma_{+,\pm} < 0$) and the non-leading poles $p_{-,\pm}$ satisfy $2\sigma_0 < \sigma_{-,\pm} < \sigma_0$.

For $r = 1$, the hyperbolas degenerate to have a focal distance of zero ($\varepsilon = 0$) and vertices coincident with its center ($\alpha = 0$) at $\sigma_0 = -\omega_c$, i.e., two crossing lines.

For $1 < r$, we have a conjugate "East–West" hyperbola, whose equation is identical to (29), except with a -1 on the right side.

Fig. 8 shows pole loci for all of the considered filters. Fig. 9 shows corresponding magnitude responses. Finally, Fig. 10 shows time-domain responses to a sawtooth wave.

4.2. Stability analysis

The generalized filter is stable when

$$\sigma_{\pm,\pm} < 0, \quad \forall \omega_c, \hat{k}, r. \tag{30}$$

As before, we can consider only the positive leading pole $p_{+,+}^{\mathrm{Ge}}$:

$$\sigma_{+,+} < 0. \tag{31}$$

This condition is satisfied for $0 \leq \hat{k} < 1$ and $0 \leq r$.

4.3. Dependence of leading pole frequency on $\hat{k}$

One way to characterize the proposed family of filters is to study how the leading pole's frequency differs from the design cutoff frequency ω_c for different amount of global feedback $\hat{k}$.

Recall that the pair $p_{+,+}^{\mathrm{Ge}}$ and $p_{+,-}^{\mathrm{Ge}}$ are the "leading" poles, i.e., the ones that are always closest to the imaginary axis $\sigma \equiv 0$. As before, we arbitrarily choose $p_{+,+}^{\mathrm{Ge}}$ to study. The real and imaginary parts of $p_{+,+}^{\mathrm{Ge}}$ are

$$\sigma_{+,+} = \omega_c \left[\sqrt{|\sigma_1 + \omega_1 j| + \omega_1^2}/\sqrt{2} - r \right] \tag{32}$$

$$\omega_{+,+} = \omega_c \sqrt{|\sigma_1 + \omega_1 j| - \omega_1^2}/\sqrt{2}. \tag{33}$$

From here we can solve for the frequency f_ℓ and quality factor Q_ℓ of the leading pole[8]. Recalling that $Q = 1/2r$, we find

$$\omega_\ell = \omega_c \sqrt{r^2 - \sqrt{2}r\sqrt{\sigma_1 + |\sigma_1 + \omega_1 j|} + |\sigma_1 + \omega_1 j|} \tag{34}$$

$$Q_\ell = \frac{\sqrt{r^2 - \sqrt{2}r\sqrt{\sigma_1 + |\sigma_1 + \omega_1 j|} + |\sigma_1 + \omega_1 j|}}{2r - \sqrt{2}\sqrt{\sigma_1 + |\sigma_1 + \omega_1 j|}}. \tag{35}$$

Here, ω_ℓ is the "undamped natural frequency" in radians and Q_ℓ

---

[8]the subscript ℓ indicating "leading"
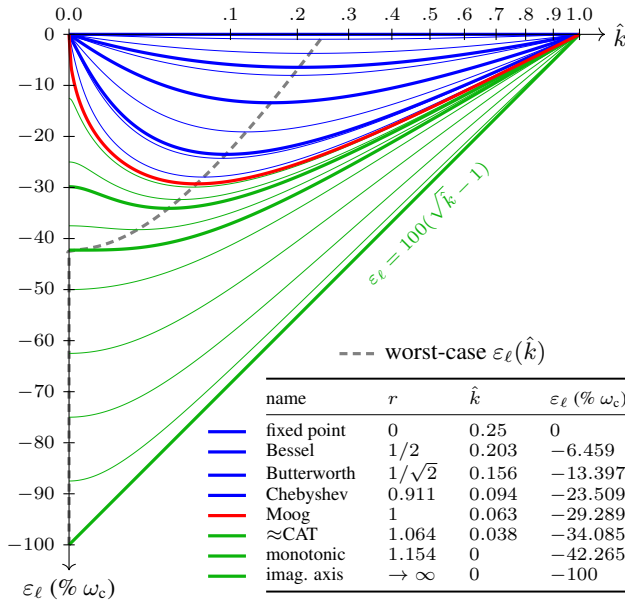
Figure 11: *Pole frequency error ε_ℓ as a function of $\hat{k} \in [0, 1]$.*

is the "pole angle" [4]. We define a pole angle error [8]

$$\varepsilon_\ell = \omega_\ell - \omega_c . \tag{36}$$

ε_ℓ is shown as a function of $\hat{k}$ for all the considered filters in Fig. 11. Here we see more differences among the filters: the shape of their leading pole frequency error, including its value at $\hat{k} = 0$, its minimum, the value of $\hat{k}$ that reaches that minimum, and its monotonicity (or lack thereof) in $\hat{k}$.

$\varepsilon_\ell = 0$ when $\hat{k} = 1 \, \forall r$, but for $\hat{k} = 0$ only for $r \leq 1$. So, if we want the error of the pole position to go to zero when $\hat{k}$ approaches zero or one, we also need $r \leq 1$. The condition $r \leq 1$ is the same as the condition to keep our hyperbola as a North–South hyperbola. In general, increasing r increases $\varepsilon_\ell \, \forall \hat{k}$. The minimum of ε_ℓ is different for different values of r and is indicated with a dashed line (- - -).

5. CONTINUOUS-TIME STATE SPACE

Many approaches to virtual analog modeling of circuits exist, including Wave Digital Filters [33, 34, 36–38], state-space modeling [13, 39, 40], and port-Hamiltonian modeling [35, 41]. Here, we have specified the filter in continuous time as a network of integrators rather than as an analog circuit. We discretize the differential equation describing that network directly.

The considered filters have continuous-time state space

$$\frac{\mathrm{d}}{\mathrm{d}t}\mathbf{v}(t) = \omega_c \mathbf{A}(t)\mathbf{v}(t) + \omega_c \mathbf{B}(t)x_{\text{in}}(t) \tag{37}$$

$$y_{\text{out}}(t) = \mathbf{C}(t)\mathbf{v}(t) \tag{38}$$

with $\{\mathbf{A}, \mathbf{B}, \mathbf{C}\}$ replaced by

$$\mathbf{A}^{\text{Ge}} = \begin{bmatrix} -2r & 1 & 0 & 4\hat{k}r^2 \\ -1 & 0 & 0 & 0 \\ 0 & -1 & -2r & 1 \\ 0 & 0 & -1 & 0 \end{bmatrix} \quad \mathbf{B}^{\text{Ge}} = \begin{bmatrix} 1 & 0 & 0 & 0 \end{bmatrix}^\top$$
$$\mathbf{C}^{\text{Ge}} = \begin{bmatrix} 0 & 0 & 0 & -\gamma_0 \end{bmatrix}$$

for the proposed generalized filter and

$$\mathbf{A}^{\text{Mg}} = \begin{bmatrix} -1 & 0 & 0 & -4\hat{k} \\ 1 & -1 & 0 & 0 \\ 0 & 1 & -1 & 0 \\ 0 & 0 & 1 & -1 \end{bmatrix} \quad \mathbf{B}^{\text{Mg}} = \begin{bmatrix} 1 & 0 & 0 & 0 \end{bmatrix}^\top$$
$$\mathbf{C}^{\text{Mg}} = \begin{bmatrix} 0 & 0 & 0 & 1 \end{bmatrix}$$

for the Moog filter. In both, x_{in}, y_{out}, and $\mathbf{v}$ represent the filter input, output and state vector, respectively.

5.1. Matching the Moog and Octave CAT filters

Despite their differing signal flow structures, the proposed generalized model can, even in continuous time, exactly match the time-varying behavior of the Moog filter. The specific case of the proposed generalized filter evaluated at $r = 1$ and $\gamma_0 = -1$, which accomplishes this, is denoted by $\{\hat{\mathbf{A}}^{\text{Ge}}, \hat{\mathbf{B}}^{\text{Ge}}, \hat{\mathbf{C}}^{\text{Ge}}\}$.

The state-space formulation of the Moog filter is related to the "hatted" model by a change-of-variable relationship

$$\mathbf{A}^{\text{Mg}} = \mathbf{T}\hat{\mathbf{A}}^{\text{Ge}}\mathbf{T}^{-1} , \quad \mathbf{B}^{\text{Mg}} = \mathbf{T}\hat{\mathbf{B}}^{\text{Ge}} , \quad \mathbf{C}^{\text{Mg}} = \hat{\mathbf{C}}^{\text{Ge}}\mathbf{T}^{-1} \tag{39}$$

where the similarity transform, whose entries are all $\in \{0, \pm 1\}$, is

$$\mathbf{T} = \mathbf{T}^{-1} = \text{diag}(\mathbf{T}_0, \mathbf{T}_0) \quad \text{where} \quad \mathbf{T}_0 = \begin{bmatrix} 1 & -1 \\ 0 & -1 \end{bmatrix} . \tag{40}$$

Thus, following [13, §7.5], we have

$$\mathbf{v}^{\text{Mg}}(t) = \mathbf{T}\hat{\mathbf{v}}^{\text{Ge}}(t) \quad \text{and} \quad y_{\text{out}}^{\text{Mg}}(t) = \hat{y}_{\text{out}}^{\text{Ge}}(t) . \tag{41}$$

This shows that the output of the Moog is identical to the output of our generalized model when $r = 1$ and $\gamma_0 = -1$. Since $\mathbf{T}$ is constant and does not depend on $\hat{k}$ or ω_c, this result holds even with $\hat{k}$ and ω_c varying over time.

6. DIGITAL IMPLEMENTATION

Following the method of [13, §7.14], we obtain the following state-space difference equations:

$$\mathbf{v}[n] = \widetilde{\mathbf{A}}\mathbf{v}[n-1] + \widetilde{\mathbf{B}}x_{\text{in}}[n] \tag{42}$$

$$y_{\text{out}}[n] = \widetilde{\mathbf{C}}\mathbf{v}[n-1] + \widetilde{\mathbf{D}}x_{\text{in}}[n] \tag{43}$$

where, defining $\mathbf{H} = g\left(\mathbf{I} - g\mathbf{A}\right)^{-1}$ which appears throughout,

$$\widetilde{\mathbf{A}} = 2\mathbf{H}\mathbf{A} + \mathbf{I} \qquad \widetilde{\mathbf{B}} = 2\mathbf{H}\mathbf{B}$$
$$\widetilde{\mathbf{C}} = \mathbf{C}\left(\mathbf{H}\mathbf{A} + \mathbf{I}\right) \qquad \widetilde{\mathbf{D}} = \mathbf{C}\mathbf{B} ,$$

$\mathbf{I}$ is the 2×2 identity matrix, and

$$g = \begin{cases} 2\omega_c/T & \text{typically} \\ \tan\left(2\omega_c/T\right) & \text{"warped" to match frequency } \omega_c \end{cases} .$$

Here $x_{\text{in}}[n]$, $y_{\text{out}}[n]$, and $\mathbf{v}[n]$ represent the filter input, output and state vector, respectively. $\mathbf{A}$, $\mathbf{B}$, and $\mathbf{C}$ are substituted with $\{\mathbf{A}^{\text{Ge}}, \mathbf{B}^{\text{Ge}}, \mathbf{C}^{\text{Ge}}\}$ or $\{\mathbf{A}^{\text{Mg}}, \mathbf{B}^{\text{Mg}}, \mathbf{C}^{\text{Mg}}\}$. The parameter g is the frequency-warped integrator gain [13, 37, 42, 43].

7. CONCLUSIONS

We introduced a new continuous-time filter design made from integrators, sums, and gains. It is parameterized by the damping of two state-variable filters, a global feedback amount, and a cutoff frequency. Certain dampings recover the classic Moog ladder filter and approximate the Octave CAT filter, while others create novel designs. Interestingly, we can control the degree to which passband attenuation is linked to resonance, a known but previously uncontrollable aspect of the Moog filter.

The proposed generalized filter (where $r_{1:2} = r_{2:2}$) is close enough the Octave CAT filter ($r_{1:2} \approx r_{2:2}$) to yield good intuition. Future work could study the case of $r_{1:2} \not\approx r_{2:2}$ in more detail. The case of different cutoff frequencies per stage could be interesting. Hutchins gave some initial investigations in [44].

r changes the filter's response and how it varies with $\hat{k}$, specifically the range of passband gains g_{dc}. Passband gain variation in the Moog filter has been known for a long time [20] and could be considered either a unique positive, or a defect [8]. The proposed generalized filter gives us one way to enhance or reduce this effect.

8. ACKNOWLEDGMENTS

9. REFERENCES

[1] R. A. Moog, "A voltage-controlled low-pass high-pass filter for audio signal processing," in *Proc. 17th Annu. Meeting Audio Eng. Soc.*, New York, NY, Oct. 1965, Preprint # 413.

[2] R. A. Moog, "Electronic high-pass and low-pass filters employing the base to emitter diode resistance of bipolar transistors," Oct. 1969.

[3] T. Stilson and J. O. Smith III, "Analyzing the Moog VCF with considerations for digital implementation," in *Proc. Int. Comput. Music Conf.*, Hong Kong, Aug. 1996.

[4] T. S. Stilson, *Efficiently-variable non-oversampled algorithms in virtual-analog music synthesis—A root-locus perspective*, Ph.D. diss., CCRMA, Stanford Univ., CA, June 2006.

[5] S. D'Angelo and V. Välimäki, "An improved virtual analog model of the Moog ladder filter," in *Proc. IEEE Int. Conf.Acoust., Speech Signal Process.*, Vancouver, Canada, May 2013.

[6] A. Huovilainen, "Non-linear implementation of the Moog ladder filter," in *Proc. 7th Int. Conf. Digital Audio Effects*, Naples, Italy, Oct. 2004, pp. 61–64.

[7] P. Daly, "A comparison of virtual analogue Moog VCF models," MSc. thesis, Univ. Edinburgh, Edinburgh, UK, Aug. 2012.

[8] S. D'Angelo and V. Välimäki, "Generalized Moog ladder filter: Part I – Linear analysis and parameterization," *IEEE/ACM Trans. Audio, Speech, Language Process.*, vol. 22, no. 12, pp. 1825–1832, Dec. 2014.

[9] S. D'Angelo and V. Välimäki, "Generalized Moog ladder filter: Part II—Explicit nonlinear model through a novel delay-free loop implementation method," *IEEE/ACM Trans. Audio, Speech, Language Process.*, vol. 22, no. 12, pp. 1873–1883, Dec. 2014.

[10] B. Hutchins, "A few more notes on polygon filters," *Electronotes*, vol. 11, no. 97, pp. 9–10, Jan. 1979.

[11] R. Bjorkman, "A brief note on polygon filters," *Electronotes*, vol. 11, no. 97, pp. 7–9, Jan. 1979.

[12] B. Hutchins, "A four, six, and eight-pole polygon voltage-controlled filter," *Electronotes*, vol. 11, no. 97, pp. 10–17, Jan. 1979.

[13] V. Zavalishin, *The art of VA filter design*, Oct. 2018, rev. 2.1.0.

[14] Curtis Electromusic Specialties, "CEM3320 datasheet," 1980.

[15] Solid State Micro Technology for Music, Inc., "SSM2040 datasheet," Santa Clara, CA, 1981.

[16] Sequential Circuits, Inc., "Prophet-5 synthesizer technical manual," 1982.

[17] Oberheim Electronics, "OB-Xa service manual," June 1982.

[18] Roland Corp., "JP-4 service notes," 1981.

[19] F. Fontana and M. Civolani, "Modeling of the EMS VCS3 voltage controlled filter as a nonlinear filter network," *IEEE Trans. Audio, Speech Language Process.*, vol. 18, no. 4, pp. 760–772, May 2010.

[20] B. Hutchins, "A four pole voltage-controlled network: Analysis, design, and application as a low-pass VCF and a quadrature VCO," *Electronotes*, vol. 6, no. 41, pp. 1–7, July 1974.

[21] B. Hutchins, "Voltage-controlled high-pass filters and other VCF structures," *Electronotes*, vol. 7, no. 58, pp. 14–22, Oct. 1975.

[22] B. Hutchins, "Voltage-controlled high-pass filters and other VCF structures (appendices)," *Electronotes*, vol. 7, no. 59, pp. 16–19, Nov. 1975.

[23] D. P. Rossum, "Circuit for dynamic control of phase shift," July 1976.

[24] D. Rossum, "Two IC's for electronic music," *Electronotes*, vol. 9, no. 78, pp. 15–22, June 1977.

[25] Octave Electronics Inc., "Octave CAT SRM service manual," Long Island City, NY, ca. Aug. 1978

[26] J. Allaert, "Designing voltage controlled filters for synthesizers with the SSI2164," Appl. Note AN701, Sound Semiconductor, Standard, CA, July 2019.

[27] Nippo Gakki Co., LTD, "Yamaha CS series synthesizer servicing guide," Hamamatsu, Japan, 1977.

[28] Roland Corp., "JP-6 service notes," June 1983.

[29] N. Keller, "CAT SRM synthesizer, revised: N Keller 2013 as per SN:3866," online, 2013.

[30] F. Fontana, "Preserving the structure of the Moog VCF in the digital domain," in *Proc. Int. Comput. Music Conf.*, Copenhagen, Denmark, Aug. 2007, pp. 291–294.

[31] B. Hutchins, "Additional design ideas for voltage-controlled filters," *Electronotes*, vol. 10, no. 85, pp. 5–17, Jan. 1978.

[32] B. Hutchins, "Two pole vs. four-pole filters—The issues," *Electronotes (Application Note)*, , no. 349, pp. 1–8, Aug. 1998.

[33] K. J. Werner, W. R. Dunkel, M. Rest, M. J. Olsen, and J. O. Smith III, "Wave digital filter modeling of circuits with operational amplifiers," in *Proc. 24th Europ. Signal Process Conf.*, Budapest, Hungary, Aug.–Sept. 2016, pp. 1033–1037.

[34] Ó. Bogason and K. J. Werner, "Modeling circuits with operational transconductance amplifiers using wave digital filters," in *Proc. 20th Int. Conf. Digital Audio Effects*, Edinburgh, UK, Sept. 2017, pp. 130–137.

[35] R. Müller and T. Hélie, "A minimal passive model of the operational amplifier: Application to Sallen-Key analog filters," in *Proc. 22nd Int. Conf. Digital Audio Effects*, Birmingham, UK, Sept. 2019.

[36] K. J. Werner, A. Bernardini, J. O. Smith, and A. Sarti, "Modeling circuits with arbitrary topologies and active linear multiports using wave digital filters," *IEEE Trans. Circuits Syst. I: Reg. Papers*, vol. 65, no. 12, pp. 4233–4246, Dec. 2018.

[37] K. J. Werner, *Virtual analog modeling of audio circuitry using wave digital filters*, Ph.D diss., CCRMA, Stanford Univ., CA, Dec. 2016.

[38] A. Fettweis, "Wave digital filters: Theory and practice," *Proc. IEEE*, vol. 74, no. 2, pp. 270–327, Feb. 1986.

[39] D. T. Yeh, J. S. Abel, and J. O. Smith, "Automated physical modeling of nonlinear audio circuits for real-time audio effects—Part I: Theoretical development," *IEEE Trans. Audio, Speech, Language Process.*, vol. 18, no. 4, pp. 728–737, May 2010.

[40] M. Holters and U. Zölzer, "A generalized method for the derivation of non-linear state-space models from circuit schematics," in *Proc. Europ. Signal Process. Conf.*, Nice, Italy, Aug.–Sept. 2015.

[41] A. Falaize and Thomas Hélie, "Passive guaranteed simulation of analog audio circuits: A port-Hamiltonian approach," *Appl. Sci.*, vol. 6, no. 10, 2016, article #273.

[42] F. G. Germain and K. J. Werner, "Design principles for lumped model discretisation using Möbius transforms," in *Proc. 18th Int. Conf. Digital Audio Effects*, Trondheim, Norway, Nov.–Dec. 2015, pp. 371–378.

[43] J. O. Smith III, *Physical audio signal processing for virtual musical instruments and audio effects*, W3K Publ., 2010.

[44] B. Hutchins, "The effect of feedback on four-pole filters with differing pole frequencies," *Electronotes*, vol. 11, no. 105, pp. 3–12, Sept. 1979.